IRAQI JOURNAL OF APPLIED PHYSICS
Vol. 22, No. 1, January-March 2026, pp. 31-38

Electrical and Structural Properties of $LiNi_{0.5}Fe_2O_4$ Nanoparticles Synthesized by Sol-Gel Self-Combustion Technique under Different Calcination Temperatures

Enas M. Ali
Sema N. Abdulghani *
Mohammad G. Ibrahim

Department of Physics,
College of Education for Pure Sciences,
University of Kirkuk,
Kirkuk, 36001, IRAQ
* Corresponding author:
semanizam@uokirkuk.edu.iq

Lithium nitrate, nickel nitrate, and ferric nitrate are utilized as precursors, with citric acid acting as a chelating agent. Li-Ni ferrite ($LiNi_{0.5}Fe_2O_4$) nanoparticles were manufactured via the sol-gel auto-combustion method. The synthesis technique was followed by calcination at temperatures of 400°C, 600°C, and 800°C. The impact of calcination temperatures on the crystalline structure, surface morphology, and dielectric properties of $LiNi_{0.5}Fe_2O_4$ nanoparticles was methodically examined. X-ray diffraction (XRD) test verified the existence of a single-phase cubic spinel structure. The crystallite size was ascertained from the dominant peak (311). An augmentation in crystallite size was noted with elevated calcination temperatures (i.e., from as-burnt to 800°C), varying from 28.314 nm to 40.940 nm. The lattice constant attained its maximum value of 8.292 Å at 400°C, which suggests structural relaxation (i.e., partial cation redistribution) during early-stage crystallization. The Fourier-transform infrared (FTIR) spectra exhibited three unique absorption bands indicative of the nanoparticles' chemical nature. Moreover, electrical experiments revealed that both the dielectric constant and dielectric loss diminished with rising frequency at the calcination temperature of 800°C. For instance, ε' decreased from 30±0.5 (100 Hz) to 0.2±0.05 (1 MHz), while tanδ reduced from 4±0.1 to 1.5±0.05 over the same range.

Keywords: Spinel ferrites; Sol-gel auto-combustion; Dielectric properties; Crystallite size
Received: 10 May 2025; Revised: 10 July; Accepted: 17 July 2025; Published: 1 January 2026

1. Introduction

Ferrite nanoparticles are an important group of magnetic nanoparticles that have attracted great interest as a result of their widespread applications in a variety of fields, including biomedical and industrial [1]. Ferrites are highly suitable for use in electric motors, transformers, and a variety of other applications due to their distinctive magnetic properties, which include the capacity to maintain magnetism at elevated temperatures [2].

The unusual qualities of spinel lithium ferrites come from their capacity to withstand cations of many transition metals within their lattice structure. As a result, their optical, magnetic, electrical, and structural qualities could change. In particular, the compound $Li_{0.5}Fe_{2.5}O_4$ possesses extraordinary characteristics, including a square hysteresis loop, minimal dielectric loss, and high saturation magnetization. Consequently, it has the potential to be a magnetic material for the development of hybrid nano-photocatalysts [3]. Wireless communication's quick evolution in the twenty-first century has the potential to replace costly magnetic materials in the domains of antennas and rechargeable lithium-ion batteries [4] due to its high Curie temperature, elevated magnetic permeability, and affordable pricing. Ferrite nanoparticles are metal oxides that are known for their spinel structure, which is represented by the generic formula AB_2O_4. The metallic cations A and B are situated at two separate crystallographic sites: tetrahedral (A site) and octahedral (B site) [5].

Fig. (1) illustrates that the cations in both locations are coordinated to oxygen atoms at tetrahedral and octahedral positions, respectively. The chemical formula of a compound must include Fe^{3+} in order for it to be categorized as ferrite [6]. Spinel-phase nanocrystalline ferrites $Li_{0.5}$-0.5xMx$Fe_{2.5}$-0.5xO_4 (where M = Mg^{2+}, Ni^{2+}, Fe^{2+}, Co^{2+}, Cd^{2+}, Zn^{2+}, Cu^{2+}, Mn^{2+}, etc.) are one of the most prominent families of nanomaterials due to their extensive range of applications, which includes nano ferrofluids, nanomedical devices, photocatalysts, magnetic devices, microwave devices, and gas sensors [7]. The ferrimagnetism of spinel ferrite is attributed to the resultant magnetic moment, which is the result of the antiparallel alignment of magnetic moments at the A and B sites. This is expressed as $\eta^{th} = |\eta^A - \eta^B|$. The microstructure and electromagnetic properties of lithium ferrite are considerably impacted by the replacement of metal cations. Through the sol-gel auto-combustion technique, Gandomi, Peymani-Motlagh [8] synthesized $Li_{0.5}Fe_{2.5}O_4$, $LiMg_{0.5}Fe_2O_4$, and $LiNi_{0.5}Fe_2O_4$. The remanent magnetization (Mr) and saturation magnetization (Ms) of the $LiNi_{0.5}Fe_2O_4$ catalyst are diminished by the doping of Ni or Mg ions. Employed the micro-emulsion approach to produce

praseodymium-substituted nano-crystalline Li-Ni spinel ferrites with varying Pr^{3+} concentrations. The insertion of rare earth Pr^{3+} cations resulted in an increase in the saturation magnetization (MS) of 41 emu/g and the coercivity (HC) of 156.9 Oe for $LiNi_{0.5}Fe_2O_4$ [9]. Spinel ferrite nanoparticles have been synthesized using a variety of innovative methods, including chemical hydrothermal processes, radiofrequency inductively coupled plasma, Electrochemical techniques, microwave or non-chemical processing, inert gas condensation, sol-gel auto-combustion, and mechanical milling [10].

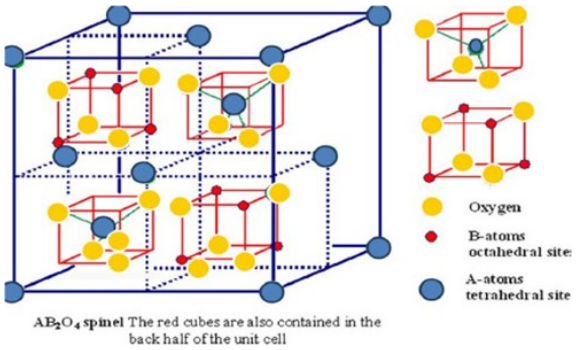

Fig. (1) Structure of spinel ferrite illustrating tetrahedral and octahedral locations [5]

The sol-gel self-combustion technique is a frequently used alternative in the creation of materials with a variety of metastable structures, even at extremely low temperatures, due to its capacity to generate products with exceptional chemical homogeneity. By modifying the preparation conditions, this method allows for the adjustment of physical properties, such as particle size, shape, and pore structure [11]. The sintering temperature is the primary factor that influences the microstructure and performance of ferrite, in addition to the training process and metal ion doping. Song, Wang [12] used the sol-gel auto-combustion approach to investigate the impact of heat treatment on $Li_{0.35}Ni_{0.3}Fe_{2.35}O_4$. They observed that with the increase in calcination temperature, a substantial increase in grain size. In terms of coercivity, it initially climbed and subsequently experienced a substantial decline from 115 to 37 Oe as the calcination temperature increased [12]. At about 600°C, the particle size approaches the transitional size between single-domain and multi-domain magnetic areas, which is the cause of this phenomenon. The sol-gel approach was employed to synthesize magnesium ferrite ($MgFe_2O_4$) nanoparticles, which were subsequently calcined at varying temperatures. The structural and magnetic properties of the nanoparticles were significantly influenced by the calcination temperature, as indicated by the results. As the calcination temperature increased, the lattice constant and crystallite size increased, whereas coercivity was reduced as a result of the reduction in the pinning effect at the grain borders [13]. The useful and practical use of lithium ferrite is significantly restricted by lithium with oxygen's volatilization at elevated sintering temperatures over 1050°C, which alters the stoichiometry of lithium ferrite and impairs its magnetic and electrical properties [14]. Therefore, while significant lithium volatilization occurs at temperatures >1050°C, a subtle L_i loss is possible at 800°C.

In this work, structural and electrical properties of $LiNi_{0.5}Fe_2O_4$, which were synthesized using the sol-gel auto-combustion procedure, were examined. Moreover, the impact of temperature fluctuations on the crystalline structure, surface morphology, and dielectric properties was methodically examined with the assistance of XRD, FTIR, FE-SEM, and LCR techniques.

2. Methodology

Magnetic nanoparticles of $LiNi_{0.5}Fe_2O_4$ were synthesized using the sol-gel auto-combustion (SGAC) technique. The precursors used included lithium nitrate ($LiNO_3$), ferric nitrate ($Fe(NO_3)_3 \cdot 9H_2O$), nickel nitrate ($Ni(NO_3)_2 \cdot 6H_2O$), citric acid ($C_6H_8O_7$), and ammonia. Analytical grades of ferric nitrate (≥99%, Sigma-Aldrich), nickel nitrate (≥99%), and lithium nitrate (≥99.9%, Sigma-Aldrich) were dissolved in deionized water, at the molar ratios of 2:0.5:1. The metal nitrate-to-citric acid ratio was carefully adjusted at room temperature, followed by the addition of liquid ammonia to neutralize the solution to a pH of 7. The resulting solution was heated on a hot plate at 100°C with continuous stirring using a magnetic stirrer to ensure complete evaporation of water. As the evaporation progressed, the solution thickened and eventually formed a very thick gel. Once the temperature increased to 200°C, the gel self-ignited, leading to the formation of a lightweight and dense powder with a large surface area, attributed to the continuation of the self-sustaining combustion reaction until complete burnout. The as-burnt powder was subsequently calcined at temperatures ranging from 400 to 800°C for 3 hours. Experimental observations indicated that all samples exhibited uniform combustion behavior, burning completely to produce fine, homogeneous powders.

3. Results and Discussion

The structural characteristics of Li-Ni ferrite ($LiNi_{0.5}Fe_2O_4$) nanoparticles were investigated using X-ray diffraction (XRD), as illustrated in Fig. (2), to determine the phase composition, crystallite size, and lattice parameters at different calcination temperatures (i.e., as-burnt, 400°C, 600°C, and 800 °C). XRD patterns exhibited eleven different peaks corresponding to crystal planes of (111), (220), (311), (222), (400), (422), (511), (440), (620), (533), and (622) within the

angular range of 2θ = 10°-80°. These peaks correspond to the characteristic reflections of the cubic spinel structure (i.e., peaks matched cubic spinel $LiFe_5O_8$ (JCPDS card no. 74-2401) with 2θ shifts <0.2° from Ni doping). As the calcination temperature rises, we observed that the intensity of these peaks amplifies, signifying improved crystallinity and phase purity. The XRD results indicate that the nanoparticles possess a single-phase cubic spinel structure, and the characteristic diffraction peaks of the ferrite's spinel phase [15,16]. The average crystallite size (D) was calculated with the Debye-Scherrer equation [17]:

$$D = \frac{k\lambda}{\beta \cos\theta} \quad (1)$$

where k is the shape factor (0.9), λ is the X-ray wavelength (0.154056 nm), β is the full-width at half maximum (FWHM) of the most intense peak, and θ is the Bragg's angle

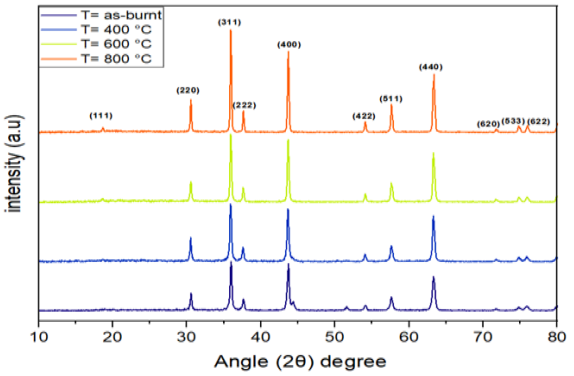

Fig. (2) XRD patterns of $LiNi_{0.5}Fe_2O_4$ NPs at various temperatures

The results show that increasing the calcination temperature results in an increase in the crystallite size from 28.314 nm (as-burnt) to 40.940 nm (800°C), suggesting enhanced crystallinity due to grain growth. Fig. (3) illustrates this trend, where a clear monotonic increase of D with an increasing temperature is observed. This is also observed in studies conducted with lithium-based spinel ferrites, in which increased temperatures are associated with reduced strain and greater crystallization [3].

From Bragg's equation, the lattice constant (a) was found together with its values showing minor fluctuations within the bounds of 8.276–8.292Å, as reported in Error! Reference source not found.). Fig. (4) illustrates this trend, a subtle increase in the lattice constant (a) with increasing temperature is likely due to the relocation of cations within the spinel lattice, which would increase the unit cell volume [18]. This might be due to the Initial Ni^{2+} migration to tetrahedral sites expands the lattice at 400°C, then oxygen vacancy formation compensates for expansion at 600°C. Finally, at 800°C, dominant crystallite growth overrides vacancy effects.

The X-ray density (ρ_{xrd}) was determined from the relation:

$$\rho_{xrd} = \frac{8M}{Na^3} \quad (2)$$

where M is the molecular weight of the sample, N is Avogadro's number, and a^3 is the unit cell volume. The ρ_{xrd} values tend to have a slight decreasing trend with an increase in temperature, as seen in Fig. (5). For instance, 5% ρ_{xrd} decrease correlates with 30% lower ε' (800°C), confirming porosity-driven property changes. This may suggest a mild reduction in atomic packing due to thermal expansion effects.

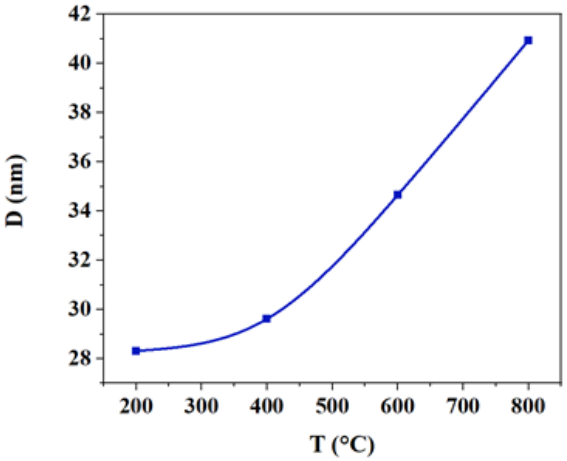

Fig. (3) Variation of crystallite size (D) with temperature

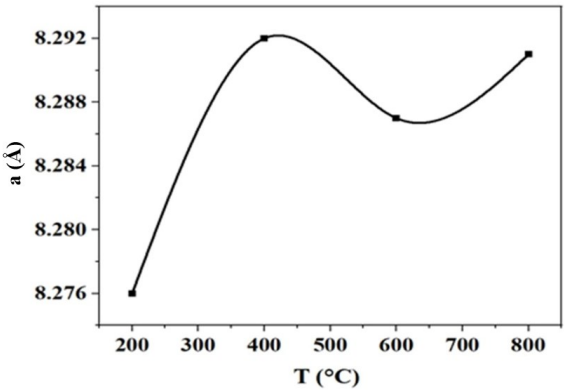

Fig. (4) Variation of lattice constant (a) with temperature

The distinct values of L_A and L_B corresponding to lattice strain have shown almost no change when measured at different temperatures, meaning that the elastic stability of the spinel phase is sustained. Fig. (6) shows that small changes of L_A and L_B are suggestive of small lattice strains, which occur quite frequently in ferrites fabricated by the sol-gel methods [19].

The microstructures of the synthesized Li-Ni ferrite samples at various temperatures of calcination (as-burnt, 400°C, 600°C, and 800°C) were analyzed by FE-SEM. As illustrated in Fig. (7), the morphology of ferrite samples ranges from spherical aggregates to irregular hexagons.

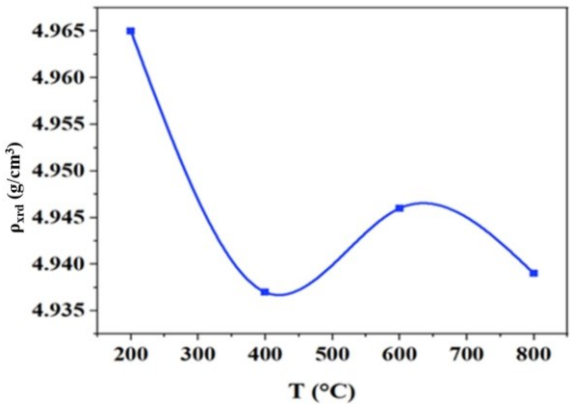

Fig. (5) Variation of X-ray density (ρ_{xrd}) with temperatures

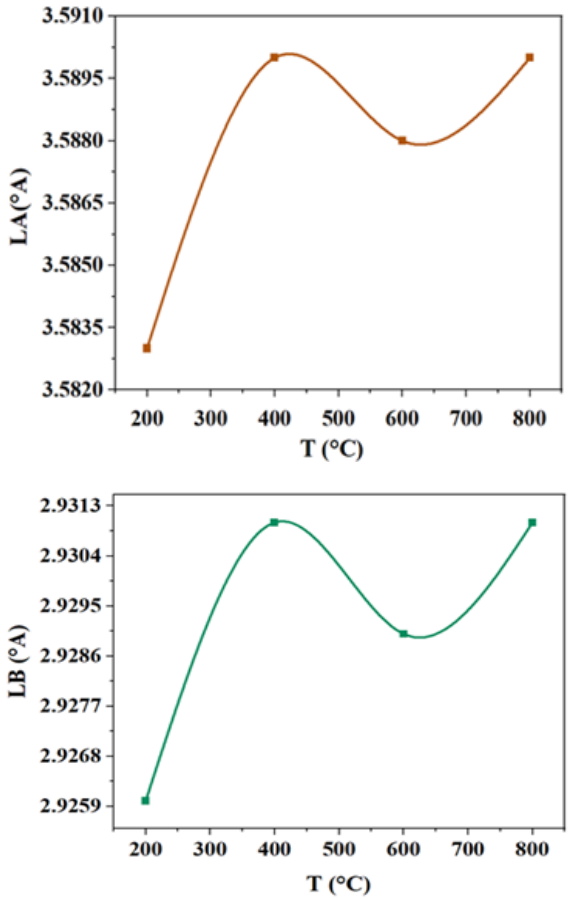

Fig. (6) Variation of L_A and L_B with temperature

The particle size distribution diagrams obtained from the particle size analyzer are illustrated in Fig. (**7**

Fig. (**8**) at different calcination temperatures (as-burnt, 400°C, 600°C, and 800°C), indicate that the grain size of the samples ranges from 29.31 to 78.62 nm. This significantly exceeds the values determined using Scherrer's formula. This could be attributed to the different ionic radii and/or clustering of the nanoparticles, which may impact the grain distribution, i.e., disorder and lattice strain of the molecular structure. Hence, the XRD method has a more stringent criterion and leads to a smaller size. Sintering often diminishes lattice imperfections and strain. Nevertheless, it will exacerbate the accumulation of crystallites, resulting in a rise in grain size, which aligns well with the trend observed in the grain size of $LiNi_{0.5}Fe_2O_4$ powder at various calcination temperatures [20].

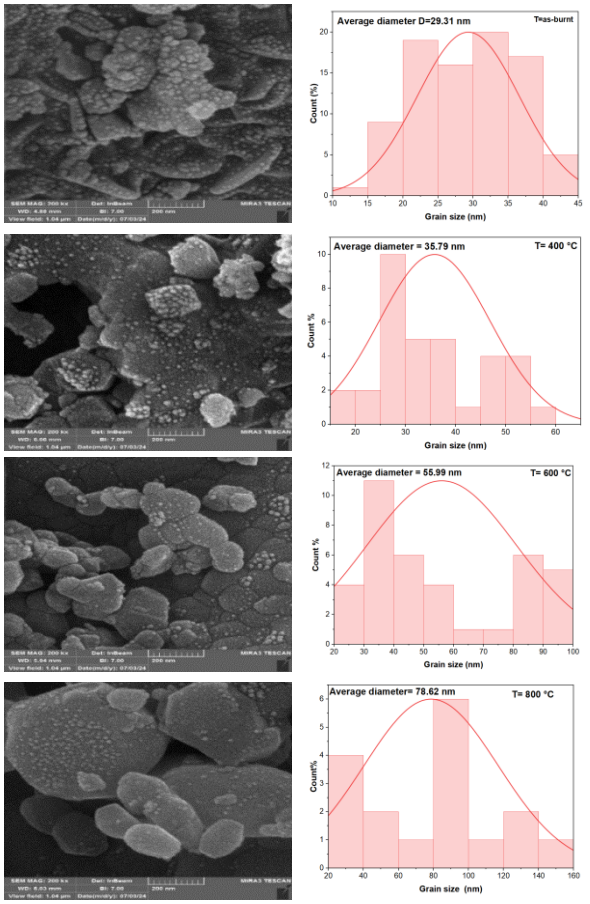

Fig. (7) FE-SEM images of $LiNi_{0.5}Fe_2O_4$ NPs at different temperatures

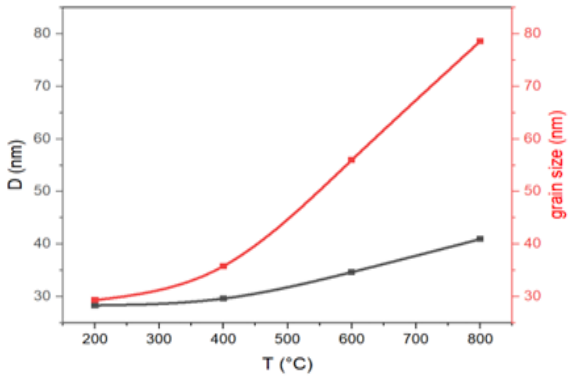

Fig. (8) Variation of crystallite size determined by X-ray and grain size of the Li-Ni ferrite at various temperatures of calcination

Fig. (9) depicts the FTIR spectra of $LiNi_{0.5}Fe_2O_4$ ferrite at various temperatures of calcination (as-burnt, 400°C, 600°C, and 800°C) in the spectral region 4000-400 cm^{-1}. FTIR spectral analysis delineates the positioning of ions in the crystal structure and supports the building of the spinel structure. All spinel compounds below 600 cm^{-1} conform to the three main absorption band vibrational modes (ν_1,ν_2,ν_3) are visible in the spectra, as shown in Error! Reference source not found.), which ν_1=523.59-526.28 cm^{-1} is characteristic of the stretching of the tetrahedral metal ion and oxygen bond, and ν_2=453.52-459.90 cm^{-1} is the characteristic for the vibration of oxygen in the direction perpendicular to the axis joining the tetrahedral ion and oxygen, which indicates the formation of a mixed spinel ferrite structure [21], and ν_1=484.27-488.31 cm^{-1} is attributed to the Li^{+}-O^{2-} complexes at octahedral site [22,23]. The frequency of the vibrations is contingent upon cation-oxygen bonding, lattice parameters, and cation mass [24]. Moreover, the incorporation of Ni into the Li ferrite reduced the wave number due to the substitution of smaller Fe^{3+} (63 pm) ions with larger Ni^{2+} (83 pm) ions [25].

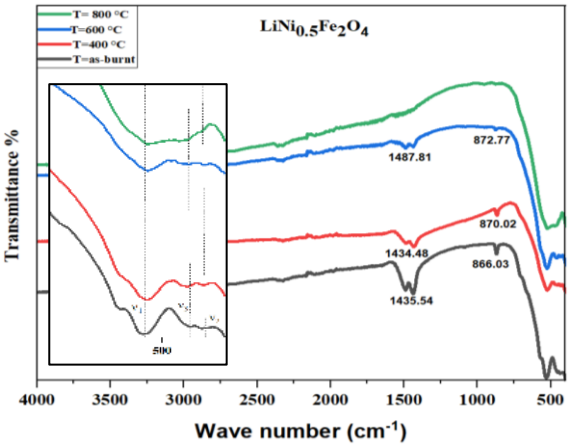

Fig. (9) FTIR spectra of $LiNi_{0.5}Fe_2O_4$ NPs for as-burnt and different calcination temperatures

Table (1) FTIR characteristic wavenumbers of $LiNi_{0.5}Fe_2O_4$ NPs for as-burnt and different calcination temperatures.

FTIR frequency bands (cm^{-1})				
Composition	T(°C)	ν_1	ν_2	ν_3
$LiNi_{0.5}Fe_2O_4$	as-burnt	523.59	453.52	488.27
	400	524.96	453.58	488.31
	600	525.42	459.68	486.33
	800	526.28	459.90	484.6

The peaks at 1434.48-1487.81 cm^{-1} and 866.03-872.77 cm^{-1} relate to metal-oxygen lattice vibrations [26], as well as the O-H stretching vibrational mode and H-O-H bonding mode, which can be attributed to the presence of free water and hydroxyl groups in the samples. As the temperature rises, the peaks associated with C-C stretching vibrations disappear [27].

The investigation of dielectric properties for ferrite nanoparticles offers insights into the electrical conduction mechanisms as reproduced in the dielectric response under an applied AC electric field. These electrical properties of ferrites are influenced by the distribution of cations between the tetrahedral and octahedral sublattices, as well as the grain size of the samples. These factors are affected by various preparation conditions and methods, including chemical composition, sintering temperature, and doping additions. The electrical properties of the $LiNi_{0.5}Fe_2O_4$ nanocomposite were examined using an LCR meter sintered at 800°C. Raising the calcination temperature to 1000°C during LCR analysis assists in improving sample quality by promoting better crystallinity, phase purity, and potentially influencing particle size and morphology, which are all crucial for accurate LCR measurements. This higher temperature can help remove impurities, reduce defects, and enhance the desired structural properties of the material. In this paper, the dielectric factors such as AC conductivity, real dielectric constant (ε'), imaginary dielectric constant (ε'') and dielectric loss angle tanδ are studied, where these parameters change with the logarithmic frequency log F (Hz) with the frequency from 100 Hz to 1 MHz [28].

The dielectric properties of ferrites are influenced by various factors, including the preparation method, the sintering processes that follow, and the distribution of cations within the sublattices, among others. The energy accumulated in the $LiNi_{0.5}Fe_2O_4$ composite is characterized by the real part of the dielectric constant (ε') when exposed to an external AC field. Ferrites exhibit frequency and temperature-dependent variations in their dielectric constant. Fig. (10) shows how the true dielectric constant varies with frequency, ranging from 100 Hz to 1 MHz. When a flashing electric field is applied, two components of the dielectric constant emerge: the real and the imaginary, which represent the stored and dissipated energy, respectively, as indicated by the relationship [29]:

$$\varepsilon = \acute{\varepsilon} - j\acute{\varepsilon} \quad (3)$$

and the dielectric constant (real part) is given by:

$$\acute{\varepsilon} = \frac{C}{C_0} \quad (4)$$

where C is the capacitance of the material, and C_0 is the capacitance of the vacuum

A high real portion of the dielectric constant (ε') is observed at low frequencies. These charges are found to be crystal defects. Space charge polarizations enhance the dielectric constant due to their slow mobility. The value decreases until it stabilizes. This is because Fe^{2+} and Fe^{3+} electrons cannot migrate effectively. As frequency increases, ε' falls. Rapid electric field direction changes do not match charge transport between Fe^{2+} and Fe^{3+}, lowering the dielectric constant [30].

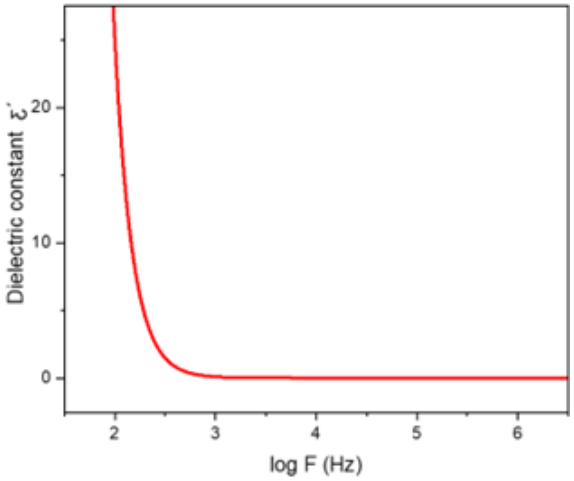

Fig. (10) Dielectric constant (ε′) as a function of frequency for Li -Ni ferrite nanoparticles sintered at 800°C

When an external AC electric field is introduced, the sample stores energy as the real component of the dielectric constant (ε′). Fig. (**10**) shows how Koop's theory and the Maxwell–Wagner model describe ferrites' dielectric phenomena at different frequencies. These models explain that ferrites have conductive grains with extremely resistant grain borders at various frequencies. Due to space charge polarization, grain boundaries enhance the dielectric constant at low frequencies. High frequencies reduce grain boundary contribution because they cannot follow electrons in a fast-changing electric field, lowering the dielectric constant.

A further significant metric is the dielectric loss, which refers to the thermal impedance of electrical energy caused by flashing current voltage in insulators. The loss factor quantifies the total core losses in nano ferrites. The AC electrical conductivity of the studied samples was measured using the AC electrical conductivity meter, and the findings were used to calculate and obtain all the parameters. Its dielectric properties and electrical conductivity in alternating current, for instance, loss tangent (tan δ), and the dielectric constant's actual value were examined in a number of frequency ranges of 50Hz-5MHz with the help of an Instek 8000G LCR meter [31]. The loss angle tangent (tanδ) and dielectric dissipation factor (ε") are crucial for assessing energy dissipation in dielectric materials under different electric fields. These two elements are related and crucial to understanding Li-Ni ferrite nanocomposite dielectric behavior. Which is calculated from the equation below:

$$\tan\delta = \frac{\varepsilon''}{\varepsilon'} \qquad (5)$$

According to Fig. (**11** and Fig. **(12**), these compounds have high (tanδ) and (ε″) at low frequencies due to space charge polarizations on very resistant grain boundaries. The evaluation of the AC ferrites' conductivity helps to understand how they conduct electricity. This is a combination of dielectric permittivity and dielectric power. The variations formed in the AC conductivity "δ_{ac}" of samples as a function of frequency are assumed in Fig. (13), and determined by the formula:

$$\delta_{ac} = 2\pi f\ \varepsilon_0\ \varepsilon'\tan\delta \qquad (6)$$

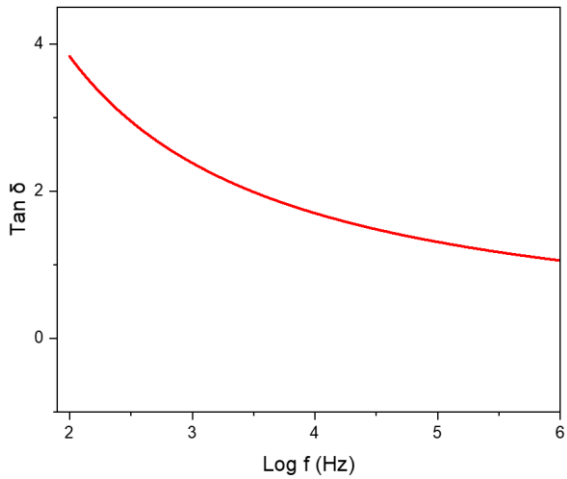

Fig. (11) Loss tangent (tanδ) as a function of frequency for Li- Ni Ferrite Nanoparticles sintered at 800°C

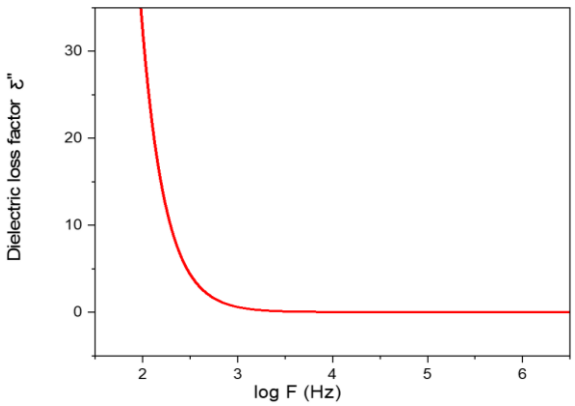

Fig. (12) Dielectric loss factor (ε″) as a function of frequency for Li- Ni ferrite NPs sintered at 800°C

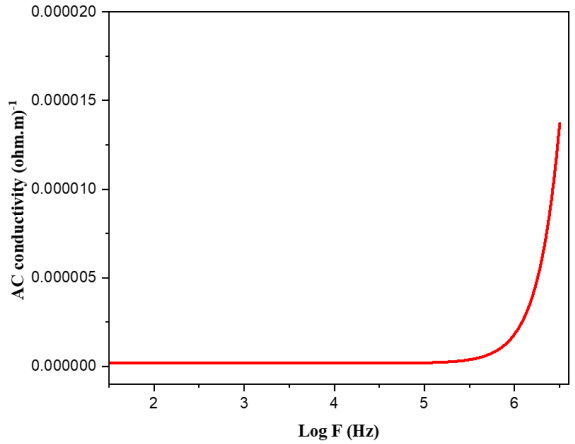

Fig. (13) Dielectric AC conductivity as a function of frequency for Li- Ni Ferrite NPs sintered at 800°C

An increase in the outer field frequency was associated with a larger AC conductivity. There is a linear relationship between frequency and AC conductivity in the low-frequency region. The greater frequency area, however, shows a sharp increase in AC conductivity. First, the significant participation of grain boundaries, which decreases charge hopping, is the reason for the linear fluctuation of AC conductivity with frequency. The decrease in grain resistivity is responsible for the dramatic rise in AC conductivity in the high-frequency region [32]. The electrical conductivity in ferrite is mainly due to the hopping of electrons between ions of the same element present in more than one valence state, distributed randomly over crystal-graphically equivalent sites.

4. Conclusions

Li-Ni ferrite nanoparticles at various calcination temperatures are synthesized by sol-gel auto-combustion technique. Li-Ni ferrite displays the cubic spinel structure, and the crystallite size was improved with the calcination temperature up to 800°C. Clear O-H and H-O-H collections were observed in strained and vibrational modes separately. The dielectric constant and dielectric loss display a reducing nature with increasing frequency, which is valuable for applications in the range of high frequency, especially in deflection yoke rings and microwave devices. On the other hand, the $LiNi_{0.5}Fe_2O_4$ nanoparticles possessed a relatively well-developed spinel structure, with an increase in crystallite size occurring parallel to the calcination temperature. The value of the lattice constant stays relatively unchanged, while the value of the X-ray density decreases moderately with an increase in temperature. This can be useful in understanding the structure of lithium nickel ferrites and their use as electrical and photocatalytic materials.

References

[1] R. Umashankara Raja et al., "The structural, magnetic and electrical properties of chromium doped calcium ferrite nanoparticles", *Chem. Phys. Impact*, 9 (2024) 100710.

[2] M.M. Ahmed and N. Abu-Elsaad, "Exploring the Magnetic Behavior of Ferrites: From Diamagnetism to Superparamagnetism", *arXiv preprint,* 2406 (2024) 10599.

[3] N. Askarzadeh and H. Shokrollahi, "A review on synthesis, characterization and properties of lithium ferrites", *Results Chem.*, 10 (2024) 101679.

[4] H. Zeng et al., "Lithium ferrite ($Li_{0.5}Fe_{2.5}O_4$) nanoparticles as anodes for lithium ion batteries", *RSC Adv.*, 4(44) (2014) 23145-23148.

[5] A.R. Tanna and H.H. Joshi, "Computer aided X-ray diffraction intensity analysis for spinels: hands-on computing experience", in *Proc. World Acad. Sci. Eng. Technol.*, 7(3) (2013) 334-341.

[6] K.K. Kefeni and B.B. Mamba, "Photocatalytic application of spinel ferrite nanoparticles and nanocomposites in wastewater treatment: Review", *Sustain. Mater. Technol.*, 23 (2020) e00140.

[7] H. Widatallah et al., "Structural and magnetic studies of nanocrystalline Mg-doped $Li_{0.5}Fe_{2.5}O_4$ particles prepared by mechanical milling", *J. Phys. D: Appl. Phys.*, 41(16) (2008) 165006.

[8] F. Gandomi et al., "Simple synthesis and characterization of $Li_{0.5}Fe_{2.5}O_4$, $LiMg_{0.5}Fe_2O_4$ and $LiNi_{0.5}Fe_2O_4$, and investigation of their photocatalytic and anticancer properties on hela cells line", *J. Mater. Sci.: Mater. in Electron.*, 30(22) (2019) 19691-19702.

[9] N. Kumar, R.K. Singh and P.R. Singh, "Structural, optical, and magnetic properties of Pr substituted Li–Ni Ferrites prepared by citrate - precursor method", *J. Mater. Sci.: Mater. in Electron.*, 32(8) (2021) 9886-9902.

[10] E. Khidher, "An Investigation of the Magnetic and Structural Characteristics of Li-Ni ferrite nanoparticles", *Al-Kitab J. Pure Sci.*, 9(2) (2025) 20-33.

[11] G.J. Owens et al., "Sol–gel based materials for biomedical applications", *Prog. Mater. Sci.*, 77 (2016) 1-79.

[12] J. Song, Z. Wang and Y. Gao, "Effect of heat treatment on structural and magnetic properties of Li–Ni ferrite prepared via sol–gel auto-combustion method", *J. Mater. Sci.: Mater. in Electron.*, 32(13) (2021) 17105-17114.

[13] D.H. de Hoyos-Sifuentes et al., "Synthesis and characterization of $MgFe_2O_4$ nanoparticles and PEG-coated $MgFe_2O_4$ nanocomposite", *J. Mater. Res. Technol.*, 18 (2022) 3130-3142.

[14] S. Soreto et al., "Lithium ferrite: synthesis, structural characterization and electromagnetic properties", Magnetic Spinels – Synthysis, Properties and Applications, InTech Open (2017), pp. 31-50.

[15] Z.A. Ali, A.I. Salih and A.M. Ghaleb, "Synthesis of Tin Oxide Thin Films by Sol-gel Spin Coating Method and Study of Their Color Properties Using CIE 1931 and CIE LAB systems", *Iraqi J. Appl. Phys.*, 21(1) (2025) 3-8.

[16] H.L. Andersen et al., "Crystalline and magnetic structure–property relationship in spinel ferrite nanoparticles", *Nanoscale*, 10(31) (2018) 14902-14914.

[17] S. Fatimah et al., "How to calculate crystallite size from x-ray diffraction (XRD) using Scherrer method", *ASEAN J. Sci. Eng.*, 2(1) (2022) 65-76.

[18] M.H. Badr et al., "Influence of annealing temperature on microstructure, magnetic and electrical properties of Ce doped cobalt ferrite nanoparticles", *Ceram. Int.*, 50(12) (2024) 21367-21377.

[19] V. Chaudhari et al., "Crystallographic, magnetic and electrical properties of $Ni_{0.5}Cu_{0.25}Zn_{0.25}La_xFe_{2-x}O_4$ nanoparticles fabricated by sol–gel method", *J. Alloys Comp.*, 549 (2013) 213-220.
[20] J.S. Jumaa, S.R. Saeed and A.M. Mohammad, "Synthesize $CoFe_2O_4/SiO_2$ nanoparticles and investigate their magnetic, dielectric, and structural characteristics", *Passer J. Basic Appl. Sci.*, 5(2) (2023) 278-289.
[21] A. Charles Prabakar et al., "Photocatalytic dye degradation properties of zinc copper ferrites nanoparticles", *J. Nanostruct.*, 9(4) (2019) 694-701.
[22] D. Ravinder, "Far-infrared spectral studies of mixed lithium–zinc ferrites", *Mater. Lett.*, 40(5) (1999) 205-208.
[23] P. Thakur et al., "Structural and optical properties of $Mn_{0.5}Zn_{0.5}Fe_2O_4$ nano ferrites: Effect of sintering temperature", *Mater. Chem. Phys.*, 193 (2017) 285-289.
[24] A.S. Shafaay and R. Ramadan, "The Influence of Zn Doping on the Cation Distribution and Antibacterial Activity of $CoFe_2O_4$", *J. Superconduct. Novel Magnet.*, 36(5) (2023) 1465-1480.
[25] J. Massoudi et al., "Magnetic and spectroscopic properties of Ni–Zn–Al ferrite spinel: from the nanoscale to microscale", *RSC Adv.*, 10(57) (2020) 34556-34580.
[26] I.M. Ghalib, K.A. Ziedan and M.A.R. Sabah, "Characterization of Al-Substituted Ni-Zn Ferrites by XRD and FTIR Techniques", *J. Media Culture Commun.*, 4(5) (2024) 24-39.
[27] M. Srivastava et al., "Influence of pH on structural morphology and magnetic properties of ordered phase cobalt doped lithium ferrites nanoparticles synthesized by sol–gel method", *Mater. Sci. Eng. B*, 175(1) (2010) 14-21.
[28] S. Baul et al., "Investigation of the structural, magnetic and dielectric properties of $NiFe_2O_4$/nanoclay composites synthesized via sol-gel autocombustion", *J. Mater. Res. Technol.*, 27 (2023) 6606-6618.
[29] A.M. Mohammad, S.A. Ridha and T.H. Mubarak, "Dielectric properties of Cr-substituted cobalt ferrite nanoparticles synthesis by citrate-gel auto combustion method", *Int. J. Appl. Eng. Res.*, 13(8) (2018) 6026-6035.
[30] S.M.A. Ridha, "X-ray studies and electrical properties of the zinc-substituted copper nanoferrite synthesized by sol-gel method", *Int. J. Compos. Mater.*, 5(60 (2015) 195-201.
[31] M.A. Mohammed and T.M. Awad, "Effects of Temperature, Pressure, and Frequency on Electrical Conductivity and Dielectric Behavior of PVA Nanopolymers", *Iraqi J. Appl. Phys.*, 21(2) (2025) 257-262.
[32] E.K. Al-Shakarchi et al., "Effect of Ni Content on Structural and Magnetic Properties of Li-Ni Ferrites Nanostructure Prepared by Hydrothermal Method", *J. Superconduct. Novel Magnet.*, 29(4) (2016) 923-929.

Table (2) Displays the FWHM, crystallite size, lattice constant (a), and X-Ray density (ρ_{xrd}) for each sample at different calcination temperatures

Sample	T (°C)	FWHM	D(nm)	a (°A)	ρ_{xrd}(g/cm^3)	L_A(°A)	L_B (°A)
$LiNi_{0.5}Fe_2O_4$	As-burnt	0.295	28.314	8.276	4.965	3.583	2.926
	400	0.282	29.613	8.292	4.937	3.590	2.931
	600	0.241	34.654	8.287	4.946	3.588	2.929
	800	0.204	40.940	8.291	4.939	3.590	2.931

